PCCP

Thermal Transport in Monocrystalline and Polycrystalline Lithium Cobalt Oxide

Journal:	*Physical Chemistry Chemical Physics*
Manuscript ID	CP-ART-03-2019-001585.R1
Article Type:	Paper
Date Submitted by the Author:	01-May-2019
Complete List of Authors:	He, Jinlong; Utah State University Zhang, Lin; University of Pittsburgh Liu, Ling; Utah State University,

ARTICLE

Thermal Transport in Monocrystalline and Polycrystalline Lithium Cobalt Oxide

Received 00th January 20xx,
Accepted 00th January 20xx

DOI: 10.1039/x0xx00000x

Jinlong He, [a] Lin Zhang [b] and Ling Liu [*a]

Efficient heat dissipation in batteries is important for the thermal management against thermal runway and chemical instability at elevated temperatures. Nevertheless, thermal transport processes in battery materials have not been well understood especially considering their complicated microstructures. In this study, lattice thermal transport in lithium cobalt oxide ($LiCoO_2$), a popular cathode material for lithium ion batteries, is investigated via molecular dynamics-based approaches and thermal resistance models. The $LiCoO_2$ single-crystal is shown to have thermal conductivities in the order of 100 W m^{-1} K^{-1} with strong anisotropy, temperature dependence, and size effects. By comparison, the polycrystalline $LiCoO_2$ is more isotropic with much lower thermal conductivities. The difference is caused by random grain orientations, thermal resistance of grain boundaries, and size-dependent intra-grain thermal conductivities that are unique to polycrystals. The grain boundary thermal conductance is calculated to be in the range of 7.16 - 25.21 GW m^{-2} K^{-1}. The size effects of intra-grain thermal conductivities are described by two empirical equations. Considering all of these effects, two thermal resistance models are formed to predict the thermal conductivity of polycrystalline $LiCoO_2$. The two models predict consistent thermal conductivity–grain size relationship that agrees well with molecular dynamics simulation results. The insights revealed by this study may facilitate future efforts of battery materials design for improved thermal management.

INTRODUCTION

The Li-ion battery has been widely used in electronic devices, electric vehicles and many other consumer products and engineering systems for energy storage.[1] Among the four essential components of Li-ion batteries (i.e. cathode, anode, separator and electrolyte), the cathode plays a key role in determining the capacity and voltage of batteries, for which lithium cobalt oxide ($LiCoO_2$) has been a popular choice. Despite the many advantages including excellent energy density, power density, stability and the long cycle life,[2] $LiCoO_2$ has a drawback of relatively low thermal conductivities, which may potentially cause inefficient heat dissipation leading to thermal runaway and chemical instability at elevated temperatures. Hence, it is of great importance to study thermal transport mechanisms in $LiCoO_2$ to gain more physical insights and to guide materials design for improved thermal properties.

Despite the importance, thermal transport processes in $LiCoO_2$ and other electrode materials are relatively underexplored except a few recent studies.[3,4] Many electrode materials share a common characteristic in that they have polycrystalline microstructures. $LiCoO_2$ in Li-ion batteries, for example, consist of grains with the size of 10-100 nm according to some experimental work.[5,6] The repetitive grain boundaries are thermal transport barriers as they scatter energy carriers and adversely affect the thermal conductivity. The grain boundary scattering, together with the randomly oriented grains and the size effect associated with intra-grain thermal conductivities, makes thermal transport processes in polycrystalline materials fundamentally different from that in their monocrystalline counterparts. As such, heat transfer in polycrystalline materials has attracted much attention with applications to silicon,[7-9] diamond,[9] argon,[10] graphene[11] and metallic films;[12] and grain design has been an effective approach for tuning thermal properties of materials.[13] Several models[14-17] have been developed to quantify and predict thermal conduction in polycrystals considering the effects of grain boundaries and grain sizes. These models allow accurate extrapolative predictions of thermal conductivities for polycrystals of larger grains based on the data of nanocrystalline solids. The scale-bridging models enable the use of molecular dynamics in such studies despite its length scale limitations.

Using two molecular dynamics-based computational techniques and thermal resistance models, this work systematically investigates nanoscale thermal transport processes in $LiCoO_2$ considering its monocrystal and polycrystal forms (insets of Figure 1a, b). The study of monocrystalline $LiCoO_2$ reveals the anisotropy and temperature dependence of its thermal conductivities with a discussion on the intrinsic size effects. The study of polycrystalline $LiCoO_2$ quantifies how grain size impacts on the thermal conductivity in the nanocrystalline regime. The grain boundary as an important structural component of polycrystalline $LiCoO_2$ is also studied to understand its thermal resistance for different grain orientations. All these results are integrated in two thermal resistance models for verification. Calibrated against molecular dynamics simulation results, both models provide consistent quantitative predictions of the thermal conductivity of polycrystalline $LiCoO_2$ in the full range of grain size variance.

[a] Department of Mechanical and Aerospace Engineering, Utah State University, Logan, Utah 84322, United States.
[b] Department of Mechanical Engineering and Materials Science, University of Pittsburgh, Pittsburgh, PA 15261, United States.
* Corresponding author: Ling Liu (ling.liu@usu.edu)

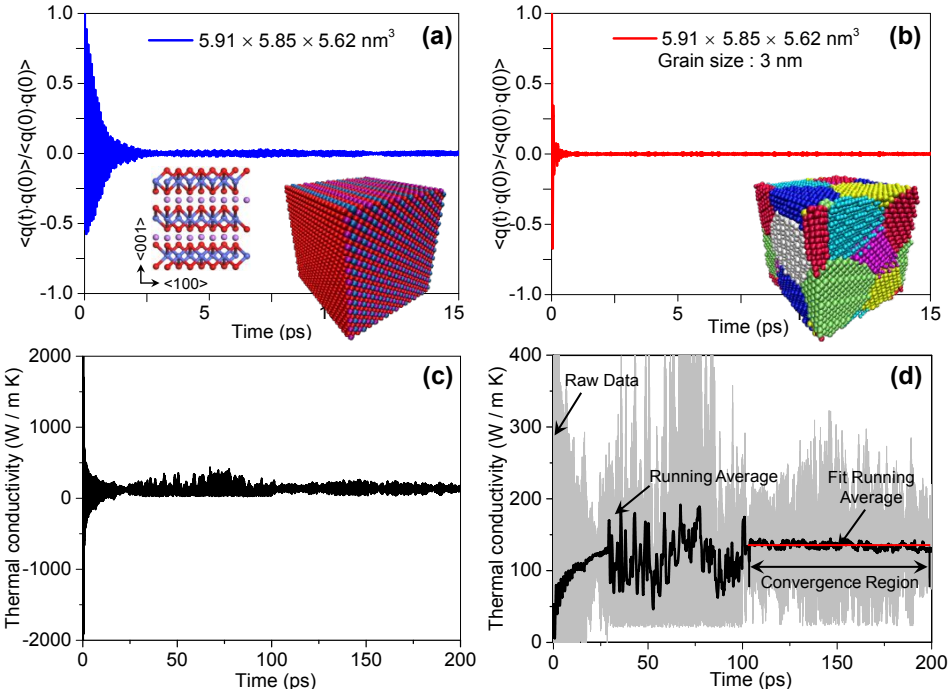

Figure 1. Representative normalized HCACF profiles of (a) a monocrystalline $LiCoO_2$ model with the box size of 5.91 × 5.85 × 5.62 nm^3 and (b) a polycrystalline $LiCoO_2$ model with the box size of 5.91 × 5.85 × 5.62 nm^3. Both HCACF profiles are along the *x*-direction or [100] for the monocrystal at 300 K. Only the first 15 ps is shown despite the total correlation time of 0.2 ns. Inset of (a) shows a side view along [010] and a 3D view of the monocrystal model. Inset of (b) shows a 3D view of the polycrystal model. (c) Raw results of the thermal conductivity by integrating the HCACF in (a), which does not converge. (d) Running average of the raw data leads to converging thermal conductivity.

MODELS AND METHODS

3D Voronoi Tessellation. Polycrystalline $LiCoO_2$ models were constructed by using the 3D Voronoi tessellation method,[18,19] which has been widely used for polycrystal modeling. Given a unit cell size for the polycrystal and a target number of grains in the unit cell, grains were randomly generated using the $LiCoO_2$ crystal structure as the structural seed. For instance, to obtain the polycrystalline $LiCoO_2$ structure with an average grain size of about 3 nm, a simulation box of 5.91 × 5.85 × 5.62 nm^3 was first divided into 8 equal cuboids and a Voronoi point was randomly generated within each of these cuboids. Then, grains boundaries were formed as planes normal to the lines linking neighboring Voronoi points. The polyhedrons bounded by these planar grain boundaries were considered as grains of the polycrystalline material. Each grain was then filled by the $LiCoO_2$ single-crystal structure at random orientations. The polycrystalline model was made fully periodical to make lattice orientation and structure both continuous across all boundaries of the simulation box. Local atomic structures at grain boundaries were further fine-tuned to fix atoms that were too close to each other (with a distance < 0.1 nm) and also to keep charges neutral.[10] The $LiCoO_2$ model formed through these steps can be found in the inset of Figure 1b.

Molecular Dynamics (MD). The $LiCoO_2$ ionic crystal was modelled by interatomic interaction along with a core-shell model to obtain reasonable dielectric constants.[20,21] The interatomic interaction energy for $LiCoO_2$ considers three terms to account for the repulsive, attractive and long-range Coulomb's forces:

$$U_{ij}\left(r_{ij}\right) = A_{ij}\exp\left(-\frac{r_{ij}}{\rho_{ij}}\right) - \frac{C_{ij}}{r_{ij}^6} + \frac{Q_i Q_j}{r_{ij}} \quad (1)$$

Here, r_{ij} is the distance between two interacting atoms, Q_i and Q_j are charges on these atoms, and A_{ij}, ρ_{ij} and C_{ij} are parameters of the potential model. The interatomic interaction is complemented by a dipolar core-shell model applied on all cobalt and oxygen ions. Each of these ions is described by a massless shell with a fractional charge *Y* and an atomic core with the rest of charge *Q*-*Y*. The core and shell are linked by a spring with the spring constant of k_{cs}. The contribution of each core-shell pair to the total energy is described by:

$$E_{cs}(s_i) = \frac{1}{2}k_{cs}s_i^2 \quad (2)$$

where s_i denotes the core-shell distance for atom *i*. For atoms represented by the core-shell model, the repulsive and attractive terms of Eq. (1) only act on the shells, while the Coulomb's term act on both cores and shells. Note that the Coulomb's interaction between core and shell of the same atom is excluded. Therefore, the total potential energy of the system takes the form of:

$$U_{total} = \sum_{i<j} U_{ij} + \sum_{i\in \mathrm{Co,O}} E_{cs} \quad (3)$$

All molecular dynamics simulations were performed using LAMMPS[22] with a time step of 1.0 fs. The short-range terms were truncated at 12 Å. The long-range Coulomb's interaction was calculated by the particle–particle particle-mesh (PPPM) method with a root mean square accuracy of 10^{-6}. Periodic boundary conditions were applied along all directions. Using the force field, MD

calculations predict that $LiCoO_2$ has the elastic moduli of 325.03 GPa, 302.09 GPa and 256.86 GPa along the three primary directions, which agree well with DFT calculations[23-25] and experimental data.[26]

Equilibrium Molecular Dynamics (EMD). Based on the fluctuation-dissipation theorem, the Green-Kubo method is an effective MD-based approach to calculate thermal conductivities of bulk materials. According to the Green-Kubo theory, the thermal conductivity tensor is proportional to a time integral of the heat current autocorrelation function (HCACF). For example, the thermal conductivity along the *i*-th (*i* = *x, y, z*) direction can be computed by:[27]

$$\kappa_i = \frac{1}{Vk_BT^2}\int_0^\infty \langle J_i(0)J_i(t)\rangle dt \tag{4}$$

where T is the temperature, k_B is the Boltzmann constant, V is the domain volume, $J_i(t)$ is the time-dependent heat current along the i-th direction, and $\langle \cdot \rangle$ represents the ensemble average. The heat flux is given by:[28]

$$\mathbf{J} = \sum_i E_i \mathbf{v}_i + \sum_{i>j}\left[\mathbf{F}_{ij}\cdot(\mathbf{v}_i+\mathbf{v}_j)\right]\mathbf{r}_{ij} \tag{5}$$

where $\mathbf{v}_i$ is the velocity of atom i, $\mathbf{F}_{ij}$ is the force on atom i exerted by its neighboring atom j, and $\mathbf{r}_{ij}$ is the relative position vector. Here, the total energy associated with the i-th atom, E_i, is expressed by

$$E_i = \frac{1}{2}m_i\mathbf{v}_i^2 + \frac{1}{2}\sum_{i\neq j}U_{ij} \tag{6}$$

where m_i is the atomic mass, and U_{ij} is the potential function defined in Eq. (1). To prepare a structure for EMD simulation, the system was first equilibrated in NPT at 300 K and 0 atm for 2 ns. The system was then simulated in NVE for 6.5 ns, with the first 2.5 ns to achieve the steady state and th e rest 4 ns for thermal conductivity calculations. To calculate thermal conductivities, a long correlation time of 0.2 ns was used in which 20000 samples of the ensemble average were obtained. Each production run of 4 ns contained 20 calculations of the integral of HCACF. Results from these calculations were averaged to reduce uncertainties.

Reverse Non-Equilibrium Molecular Dynamics (RNEMD). RNEMD[29] was used in this study to calculate: (1) interfacial thermal conductance across grain boundaries; and (2) thermal conductivity of a bulk material. The interfacial thermal conductance, G, was calculated by

$$G = \frac{J}{\Delta T} \tag{7}$$

where J is the steady-state heat flux and ΔT is the temperature drop across the grain boundary. The thermal conductivity of a bulk material along the heat flux direction (e.g. the z-direction) was calculated by

$$\kappa(L) = \frac{J}{dT/dz} \tag{8}$$

where dT/dz is the temperature gradient and J is the heat flux. The calculated κ is shown as a function of L, i.e. model length along the heat flux direction, because NEMD results are known to have prominent length effects.[30] The simulation box was divided into multiple slabs along the heat flux direction. Heat flow was generated by exchanging atomic kinetic energy between the hottest atom in heat sink and the coldest atom in heat source at specified intervals. A virtual elastic collision model was employed to maintain momentum and energy conservation during velocity swapping. At the steady state, heat flux was calculated by

$$J = \frac{\Delta E}{2tA} \tag{9}$$

where A is the cross-sectional area, ΔE is the average energy exchange per swap, t is the time interval between swaps, and the factor of "2" accounts for the two thermal transport paths form heat source to heat sink. To prepare a structure for RNEMD simulation, the systems were first optimized by conjugate gradient, then equilibrated in NPT at 300 K and 0 atm for 0.5 ns. To relax atomic structures at grain boundaries, relevant systems were heated up in NPT from 300 K to 500 K in 0.5 ns, equilibrated at 500 K and 0 atm for 0.5 ns, cooled down to 300 K in 0.5 ns, and then equilibrated at 300 K and 0 atm for 0.5 ns. Finally, the systems were simulated in NVE for 4 ns. The first 2 ns was to reach the steady state, and the latter 2 ns was the production run.

RESULTS AND DISCUSSION

Heat Current Autocorrelation. Reliable thermal conductivity calculations via EMD require convergence of the system to the steady state, which can be characterized by the normalized heat current autocorrelation function (HCACF). Figure 1a, b plots the normalized HCACF for two examples of the monocrystalline and polycrystalline $LiCoO_2$, respectively. In both plots, the normalized HCACF decays rapidly within the first couple of picoseconds. The speed of convergence is similar in the other EMD cases performed in this study. Therefore, the correlation time of 0.2 ns is sufficient for accurate thermal conductivity calculations. Compared with the monocrystalline $LiCoO_2$, the polycrystalline $LiCoO_2$ shows faster convergence in the HCACF. This can be explained by the fact that the convergence time of HCACF is proportional to the phonon mean free path or phonon relaxation time.[30] In the polycrystalline structure, phonons are dispersed across grain boundaries making the phonon mean free path restricted by the grain size. This lowers the phonon mean free path leading to faster convergence in the polycrystalline $LiCoO_2$.

An important characteristic of the HCACF of both monocrystalline and polycrystalline $LiCoO_2$ is the unmonotonous decay in the converging regime. Previous EMD studies on other materials have demonstrated two different kinds of decay in the HCACF. Some materials including silicon[9,31] and argon[10,32] show monotonous decay in the positive quadrant, while some others including quartz[33] show large oscillations between the positive and the negative as the absolute value decays. The $LiCoO_2$ falls into the second category. The large oscillations during convergence are due to the optical phonons[33] and even after convergence, there exist small oscillations or noises in the HCACF. Such oscillations make direct integration unsuitable for thermal conductivity calculations. Alternatively, McGaughey et al. proposed an approach that uses the running average to calculate thermal conductivities.[33] Figure 1c plots the thermal conductivity calculated by Eq. (4) using the autocorrelation data shown in Figure 1a. Due to oscillations present in

the autocorrelation data, the predicted thermal conductivity does not converge with time. The raw data was then treated by the running average at intervals of 200 fs. Figure 1d shows the raw data in grey and the treated data in black. Apparently the treated data has much less oscillations with a flat segment indicating convergence. An average in the convergence region gives a more accurate prediction of the thermal conductivity. This approach was applied to all EMD-based thermal conductivity calculations in this study for both monocrystalline and polycrystalline $LiCoO_2$.

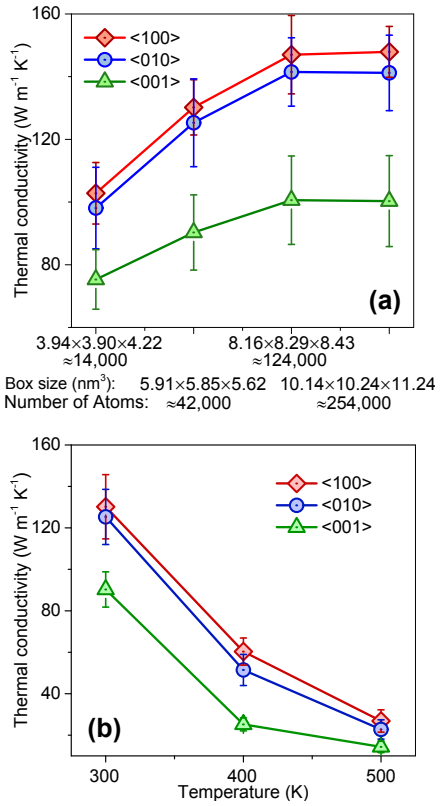

Figure 2. (a) Thermal conductivity of monocrystalline $LiCoO_2$ at 300 K along [100], [010] and [001] for four unit structures of increasing sizes. (b) Thermal conductivity of monocrystalline $LiCoO_2$ at different temperatures for the unit structure of 5.91 × 5.85 × 5.62 nm^3. Each data point is an average of the conductivities calculated from 20 independent simulations, with errors bars showing the standard deviation.

Thermal Conductivities of Monocrystalline $LiCoO_2$. This section studies the effects of three parameters (i.e. size, direction and temperature) on the thermal conductivity of monocrystalline $LiCoO_2$. Most of the results will be generated by EMD, and they will be verified against RNEMD calculations.

Thermal conductivities calculated by the Green-Kubo approach are known to have size effects. In small unit cells, phonons of longer wavelengths are prohibited which offsets thermal conductivity predictions. This effect will become insignificant when the unit cell is sufficiently large to include all important phonon modes. To understand this effect, four monocrystalline $LiCoO_2$ models of different sizes were simulated, including 3.94 × 3.90 × 4.22 nm^3, 5.91 × 5.85 × 5.62 nm^3, 8.16 × 8.29 × 8.43 nm^3 and 10.14 × 10.24 × 11.24 nm^3 which correspond to 14 × 8 × 3, 21 × 12 × 4, 29 × 17 × 6 and 36 × 21 × 8 repetitive unit cells in the simulation box. The three axes of the simulation box are aligned with the principle directions of the $LiCoO_2$ crystal, e.g. the *x*-axis along [100]. Figure 2a plots thermal conductivities of the four $LiCoO_2$ unit structures along all the three primary directions. Each data point is an average of the conductivities calculated from 20 independent simulations, with errors bars showing standard deviation. The thermal conductivity is found to increase with size along all directions with the tendency to converge. The convergence is caused by involvement of more phonon modes in larger simulation structures.

From Figure 2a, the thermal conductivity converges with the simulation box of 8.16 × 8.29 × 8.43 nm^3 since the calculation with a larger simulation box yields similar results. The converged thermal conductivity, κ_0, is 147.02 ± 12.5 W m^{-1} K^{-1}, 141.52 ± 10.9 W m^{-1} K^{-1} and 100.62 ± 14.1 W m^{-1} K^{-1} along the three directions of $LiCoO_2$. Using the phonon kinetic theory, the phonon mean free path, λ, can be estimated by

$$\kappa_0 = \frac{1}{3} C v \lambda \tag{10}$$

where *C* is the specific heat and *v* is the velocity of phonons which can be estimated by the sound velocity in the material.[34] Based on previous experiments,[35] sound velocities of $LiCoO_2$ along the longitudinal and transverse directions are 6961 m/s and 4088 m/s, respectively. An average gives *v* = 5045.67 m/s. The specific heat was calculated to be *C* = 70.52 J K^{-1} mol^{-1} at 300 K using the density functional theory.[24] Based on these results and the mean values of κ_0, Eq. (10) gives the phonon mean free path of 55.11 nm, 53.04 nm and 37.71 nm along the three direction at 300 K.

Based on the results, the thermal conductivity of monocrystalline $LiCoO_2$ is anisotropic with the ranking of [100] > [010] > [001]. This is consistent with the lattice structure of $LiCoO_2$. The $LiCoO_2$ solid is a layered structure composed of monovalent Li^+ layers and anionic Co and O layers alternating along the [001] direction (see inset of Figure 1a for detail). Phonons experience strong scattering as they transport through the alternating layers in such a "composite" layered structure, which lowers the thermal conductivity along [001]. By comparison, the atomic structure is relatively more consistent within the plane of layers, causing thermal conductivities along the two in-plane directions (i.e. [100] and [010]) comparable with each other and higher than that along [001]. In addition to the anisotropy, thermal conductivities of $LiCoO_2$ are also found to depend on temperature. As shown in Figure 2b, the thermal conductivity drops by about 60.33% from 300 °C to 400 °C, and decreases further by about 53.31% from 400 °C to 500 °C. In most single crystals, thermal conduction at elevated temperatures is increasingly influenced by the phonon-phonon Umklapp scattering, which lowers the thermal conductivity.[36,37]

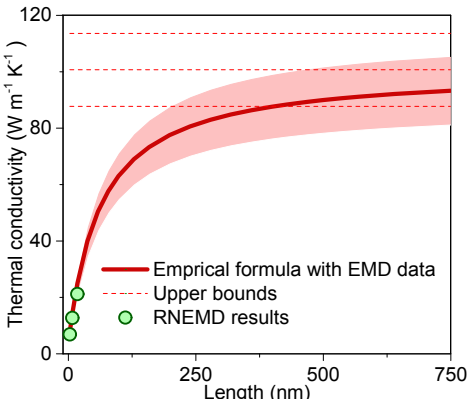

Figure 3. Size effects associated with the thermal conductivity of monocrystalline $LiCoO_2$ along the [001] direction. The curve plots the empirical equation Eq. (11) using κ_0 and λ from converged EMD calculations. The shared area is bounded by two similar curves of Eq. (11) considering the standard deviation of κ_0. The three dotted lines are the upper limit of these three curves. Green circles are RNEMD simulation results with different lengths along [001].

The EMD results were further verified by RNEMD for monocrystalline $LiCoO_2$ at 300 K. Due to the setup of RNEMD, it can only calculate the thermal conductivity along one direction at a time, and this verification considers [001]. Another important characteristic of RNEMD is that its results have strong dependency on model length along the direction of interest. One reason is the constraints imposed by the finite model size on phonons of longer wavelengths, similar to that in EMD. Another reason unique to RNEMD is caused by the varying temperature within the model leading to enhanced phonon scattering. The latter explains why for most materials, RNEMD has much more significant size effects than EMD. Based on many previous studies, the length effect of RNEMD is well characterized by the empirical equation proposed by Schelling *et al.*[30] which takes the form of

$$\frac{1}{\kappa(L)}=\frac{1}{\kappa_0}\left(\frac{\lambda}{L}+1\right) \tag{11}$$

where κ is the length-dependent thermal conductivity, L is the model length along the direction of interest, $\kappa_0=\kappa_{L\to\infty}$ is the thermal conductivity at the infinite length or when the length effect does not play a role, and λ is the phonon mean free path. The verification was done by comparing length-dependent RNEMD results with the κ-L

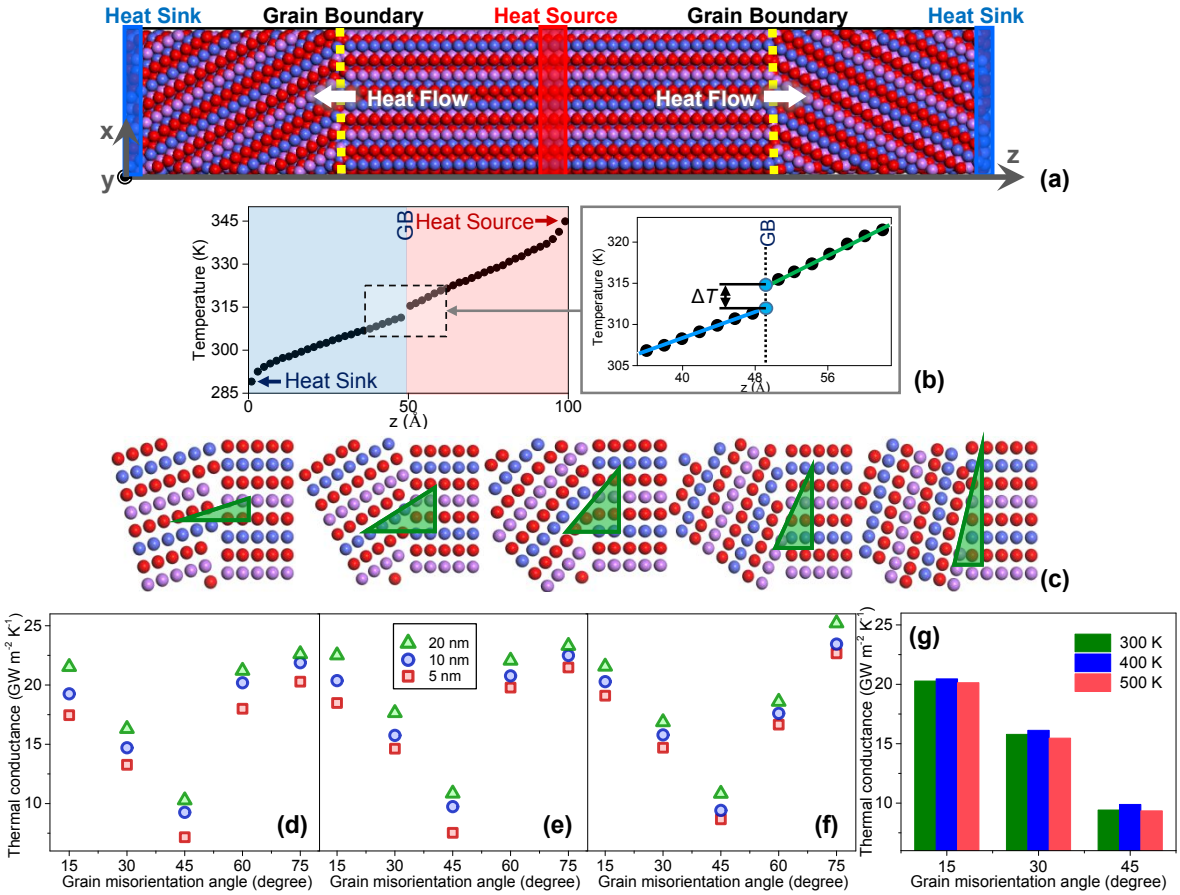

Figure 4. (a) A representative model for grain boundary thermal conductance calculations (blue spheres: cobalt; red spheres: oxygen; pink spheres: lithium). (b) Left: temperature profile of the computational system from the RNEMD simulation. Right: A temperature jump is identified across the grain boundary. (c) Five grain boundaries with different tilt angle including 15º, 30º, 45º, 60º and 75º about the *y*-axis. (d) Grain boundary thermal conductance versus the tilt angle and grain size for different tilt orientations about the (d) *x*-axis, (e) *y*-axis and (f) *z*-axis. (g) Effect of temperature on the interfacial thermal conductance for three tilt angles about the *z*-axis.

relationship predicted by Eq. (10) using κ_0 and λ from the EMD calculations. Quantitatively, along the direction of interest, i.e. [001], EMD gives κ_0 = 100.62 W m^{-1} K^{-1} and λ = 37.71 nm. With these two numbers, Eq. (11) is plotted in Figure 3 which shows excellent agreement with the RNEMD results. Note that the plot of Eq. (11) in Figure 3 also considers the uncertainties associated with κ_0. The thick red line shows the prediction made with the mean value of κ_0, while the red shaded area shows the variance bounded by predictions made considering the standard deviation of κ_0. The RNEMD results are shown as green circles for the model length of 9.84 nm, 19.68 nm and 39.35 nm along the [001] direction. In the RNEMD simulation, transverse dimensions along [100] and [010] were set as 3.38 nm and 3.41 nm, respectively, which were large enough to not affect thermal conductivity calculations along [001]. Due to the prominent size effects associated with RNEMD, thermal conductivities predicted with the given lengths are from 6.69 W m^{-1} K^{-1} to 21.01 W m^{-1} K^{-1}, far below κ_0. However, the agreement shown in Figure 3 suggest excellent consistency between the two approaches.

Grain Boundary Thermal Conductance. RNEMD was employed to study thermal transport across grain boundaries in polycrystalline $LiCoO_2$. A typical simulation model is shown in Figure 4a which contains two grains. The two grains were assumed to have the same size, *d*, which was varied among 5 nm, 10 nm and 20 nm. One grain was rotated with respect to the other to represent different grain orientations in polycrystals. The rotation can be characterized by two parameters, i.e. the rotation direction and the rotation or tilt angle. This study considers five tilt angles including 15°, 30°, 45°, 60° and 75° (Figure 4c) about the three primary axes. For each grain boundary, the RNEMD simulation leads to a temperature profile as illustrated in Figure 4b. The temperature profile is almost linear in each of the grains except for the nonlinear regions near the heat source and the heat sink. At the grain boundary, a temperature "jump", ΔT, is identified which is correlated with the grain boundary thermal conductance.

The resulting thermal conductance is plotted in Figure 4d-f for tilts about the *x*, *y* and *z*-axis, respectively. Interestingly, the tilt direction does not show significant impact on the grain boundary thermal conductance. Instead, the tilt angle plays the most important role. As the tilt angle increases from 0° to 90°, the grain boundary thermal conductance first decreases almost linearly and then increases, attaining its minimum when the tilt angle equals to 45°. Use the data for d = 20 nm as an example. The grain boundary thermal conductance is 21.53 GW m^{-2} K^{-1} when the tilt is at 15° about the *x*-axis, and it drops by 50% to 10.28 GW m^{-2} K^{-1} when the tilt is at 45°. Indeed, among all tilt angles under investigation, 45° leads to the most defects at the grain boundary, and gives the most different lattice structures along the direction of heat current between the two grains. Both factors cause significant phonon scattering and drastically increase thermal resistance. In addition to the tilt angle, the grain size is also found to influence the grain boundary thermal conductance, due to the same reasons that cause the size effects of RNEMD as shown in Figure 4. Overall, the grain boundary thermal conductance of $LiCoO_2$ is 7.16 ~ 25.21 GW m^{-2} K^{-1} considering all cases investigated in this study.

Further, effect of temperature is explored by using a representative microstructure with the grain size of 10 nm, three selected tile angles about the z-axis including 15°, 30° and 45°, and three temperatures including 300 K, 400 K and 500 K. As shown in Figure 4g, temperature does not show obvious impact on the interfacial thermal conductance, in agreement with previous theoretical studies.[38-40]

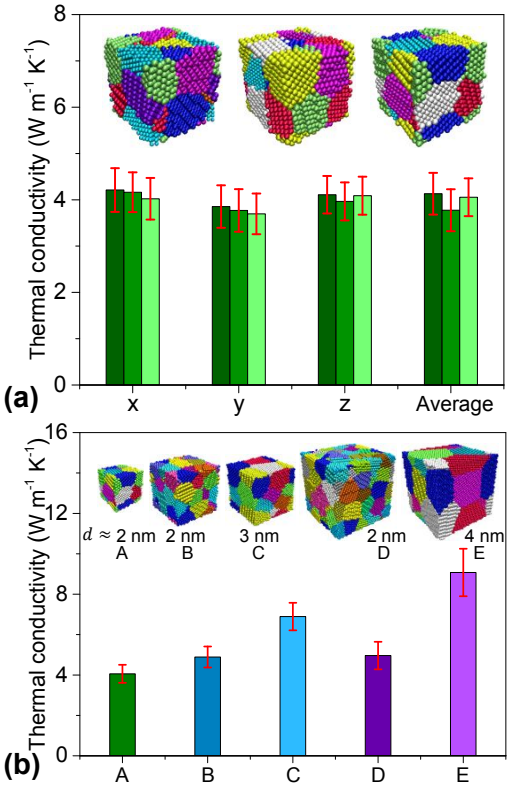

Figure 3. (a) Thermal conductivities of three polycrystalline $LiCoO_2$ models at 300 K. All three models shown in the insets have 8 grains randomly generated in a box of 3.94 × 3.90 × 4.22 nm^3. (b) Average thermal conductivity of polycrystalline $LiCoO_2$, $\bar{\kappa}$, for five models of different box sizes and numbers of grains. Insets show the five unit structures. Their grain sizes are 2.01 nm, 1.93 nm, 2.90 nm, 2.07 nm and 4.15 nm, respectively.

Thermal Conductivities of Polycrystalline $LiCoO_2$. Thermal conductivities were calculated for polycrystalline $LiCoO_2$ using unit structures randomly generated by 3D Voronoi Tessellation. Due to the randomness in unit structure sampling, it is important to understand how much variation the predicted thermal conductivity has due to the structural randomness. For this purpose, three simulation boxes were generated with the same box size of 3.94 × 3.90 × 4.22 nm^3 and the same number of grains (eight). Their thermal conductivities are shown in Figure 5a. Although 8 is not a large number of grains, the predicted thermal conductivities already show some isotropy due to the averaging effects caused by randomly oriented grains. The largest conductivity is only about 8-9% higher than the lowest for the same model. The isotropy is expected to be more apparent when more grains are present in the model. Due to the demonstrated isotropy, thermal conductivity averaged from the three directions, $\bar{\kappa}$, will be

considered in following discussion. Importantly, $\overline{\kappa}$ shows very small sample variance as the unit structure changes. For the three unit structures under investigation, $\overline{\kappa}$ is found as 4.06, 3.97 and 3.94 W m^{-1} K^{-1}, respectively, with differences below 3%. The sample variance is also expected to decrease with the number of grains.

Figure 5b shows $\overline{\kappa}$ of five representative unit structures of $LiCoO_2$ with different box sizes and grain sizes. Model A has 8 grains in the box of 3.94 × 3.90 × 4.22 nm^3. Model B has 27 grains and model C has 8 grains, both in the box of 5.91 × 5.85 × 5.62 nm^3. Model D has 64 grains and model E has 8 grains, both in the box of 8.16 × 8.29 × 8.43 nm^3. The grain sizes, d, of these five unit structures are 2.01 nm, 1.93 nm, 2.90 nm, 2.07 nm and 4.15 nm, respectively. There are two important findings:

(1) Models A, B and D have comparable grain sizes of approximately 2 nm, and their thermal conductivities are 4.06, 4.89 and 4.96 W m^{-1} K^{-1}, respectively. On one hand, these results are very close, suggesting the important role of grain size. On the other hand, the increasing trend matches well with the size effect revealed in Figure 2a for monocrystalline $LiCoO_2$. Indeed, as the number of grains increases from 8 (A) to 27 (B) and finally to 64 (D), the simulation box size increases. This allows phonons of longer wavelengths to participate in heat transfer, leading to higher thermal conductivities.

(2) Models A, C and E feature increasing grain sizes, and their thermal conductivities are 4.06, 6.89 and 9.08 W m^{-1} K^{-1}, respectively. The results, again, show the important role of grain size – the larger grain size, the higher thermal conductivity. The grain size effect will be elucidated in the next section using two thermal resistance models.

It deserves mentioning that the grains in any polycrystal have a distribution in size. As the present study mainly focuses on the effect of average grain size on the thermal conductivity of $LiCoO_2$, some studies in the literature have revealed that the grain size distribution also plays a role. In general, polycrystals with fine grains may have higher thermal conductivities when the grain size is more widely distributed; and such an effect is reduced as the average grain size increases. Using polycrystalline h-BN as an example,[41] when the average grain size is about 1 nm, the thermal conductivity with non-uniform grains is about 15% higher than that with uniform grains. The difference drops below 1% when the average grain size exceeds 200 nm. Similar trend is expected for other polycrystals including $LiCoO_2$. With fine grains, the grain boundaries dominate in thermal resistance and heat may be conducted along paths that connect larger grains to reduce thermal resistance. The effect is eliminated when the grain size is sufficiently large so that the intra-grain thermal resistance dominates.

Thermal Resistance Models. Polycrystalline and monocrystalline $LiCoO_2$ are shown to have thermal conductivities that are 1-2 orders of magnitude different. The discrepancy is caused by the many grain boundaries in polycrystals that resist thermal conduction. This section discusses two thermal resistance models that integrate thermal conductivities of the polycrystal and monocrystal along with the thermal conductance of grain boundaries. The purposes are two folds. First, the model involves all results presented in previous sections for the monocrystal, polycrystal and grain boundaries. It will therefore serve as a verification of computational results of this study. Second, the polycrystals considered in the EMD calculations are limited to having nanoscale grains but realistic polycrystalline $LiCoO_2$ usually have larger grains. This issue can be solved by the thermal resistance models as they work for polycrystals of any grain sizes.

Simplifying the polycrystal as a linear set of grains with equal lengths connected with grain boundaries, thermal resistance model[15] gives

$$\frac{d}{\kappa_{poly}} = \frac{d}{\kappa_{grain}} + \frac{1}{G_{gb}} \tag{12}$$

where $\boldsymbol{\kappa_{poly}}$ and $\boldsymbol{\kappa_{grain}}$ are thermal conductivities of the polycrystal and the grain, respectively, G_{GB} is the grain boundary thermal conductance, and d is the grain size. It is important to note that $\boldsymbol{\kappa_{grain}}$ is not $\boldsymbol{\kappa_0}$ which is the thermal conductivity of the monocrystal. Due to the finite size of grains, $\boldsymbol{\kappa_{grain}}$ has a size effect which can be approximately described by Eq. (11). Due to randomly oriented grains in the polycrystal, $\boldsymbol{\kappa_0}$ in the equation is approximated by $\overline{\boldsymbol{\kappa_0}}$, which is an average of thermal conductivities along the three directions for monocrystalline $LiCoO_2$. Based on the converged values from the EMD simulation, $\overline{\boldsymbol{\kappa_0}}$ = 129.72 W m^{-1} K^{-1}. Similarly, $\boldsymbol{\lambda}$ is approximated by $\overline{\boldsymbol{\lambda}}$ which is 48.62 nm. Use model E in Figure 5 which has 8 grains in a box of 8.16 × 8.29 × 8.43 nm^3 as an example. Eq. (11) gives $\boldsymbol{\kappa_{grain}}$ = 10.16 W m^{-1} K^{-1} with $L = d$ = 4.15 nm. Subsequently, Eq. (12) gives G_{gb} = 20.43 GW m^{-2} K^{-1} given that the average thermal conductivity of the polycrystal is $\boldsymbol{\kappa_{poly}}$ = 9.08 W m^{-1} K^{-1} based on the EMD results. The result of grain boundary thermal conductance is well within the range of 7.16 ~ 25.21 GW m^{-2} K^{-1} predicted by RNEMD, which verifies the results of this study.

A more recent model[17] expresses κ_{grain} as $Cv\lambda_{grain}/3$ following Eq. (10) and uses the Matthiessen's rule[42] of $\lambda_{grain}^{-1} = \lambda_0^{-1} + \lambda_{gb}^{-1}$

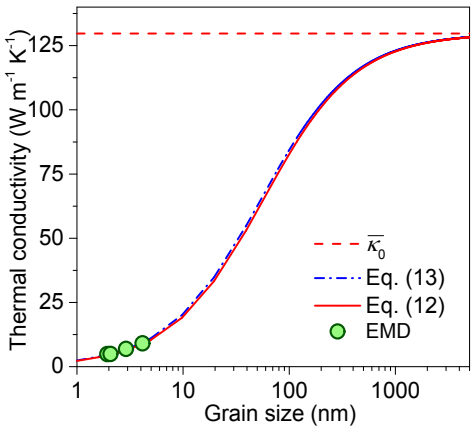

Figure 4. Average thermal conductivity, $\overline{\boldsymbol{\kappa}}$, of polycrystalline $LiCoO_2$ versus grain size. The red line plots Eq. (12) with the size effects described by Eq. (11). The blue dash-dotted line plots Eq. (13), which is fitted using the EMD results (green circles). Both models predict the thermal conductivity of polycrystalline $LiCoO_2$ and converge to $\overline{\boldsymbol{\kappa_0}}$, the average thermal conductivity of monocrystalline $LiCoO_2$ (red dashed line).

where λ_{grain} and λ_{gb} are phonon mean free path of the grain and the additional phonon mean free path caused by grain boundaries. Assuming λ_{gb} scales with d^{α}, the model takes the form of

$$\kappa_{poly} = \frac{\kappa_0 \Big/ \left(1+\lambda d^{-\alpha}\right)}{1+\kappa_0 \Big/ \left[\left(1+\lambda d^{-\alpha}\right) G_{gb} d\right]} \quad (13)$$

where α is a fitting parameter. The fitting is based on EMD results of the thermal conductivity for polycrystals of various grain sizes. For each polycrystal model, $\boldsymbol{\kappa_{poly}}$ is calculated by averaging thermal conductivities along the three directions and d is the corresponding grain size. $\boldsymbol{\kappa_0}$ and $\boldsymbol{\lambda}$ are approximated by $\boldsymbol{\kappa_0}$ and $\overline{\boldsymbol{\lambda}}$. G_{gb} is approximated as 16 GW m^{-2} K^{-1}, which is right in the middle of the range calculated by RNEMD. The fitting gives $\alpha = 0.9961$ for $LiCoO_2$ with a correlation factor of 0.95. The equation with this α is plotted in Figure 6 as the blue dash-dotted line, while the EMD data used for fitting is shown by green circles. As the grain size increases, the predicted $\boldsymbol{\kappa_{poly}}$ approaches $\boldsymbol{\kappa_0}$. Similar prediction can also be made by the first model using Eq. (12) together with Eq. (11) and the same G_{gb} = 16 GW m^{-2} K^{-1}. The resulting $\boldsymbol{\kappa_{poly}}$ is plotted in Figure 6 as the red solid line. Both models give excellent agreement with each other.

A recent experimental work measured the thermal conductivity of polycrystalline $LiCoO_2$ as 5.4 W m^{-1} K^{-1}.[26] The cross-sectional high-resolution transmission electron microscopy (HRTEM) image[26] shows that the average grain size is below 10 nm. Assuming a grain size of 5 nm, our model shown in Eq. (13) predicts the thermal conductivity of 10.45 W m^{-1} K^{-1}. The difference is attributable to imperfections present in the sample due to the relatively low annealing temperature of 500 °C.[26]

CONCLUSIONS

To summarize, this work uses the MD simulation in combination with thermal resistance models to understand thermal transport in monocrystalline and polycrystalline $LiCoO_2$ and across its grain boundaries. The monocrystalline $LiCoO_2$ shows anisotropic thermal conductivities of 147.02 ± 12.5 W m^{-1} K^{-1}, 141.52 ± 10.9 W m^{-1} K^{-1} and 100.62 ± 14.1 W m^{-1} K^{-1} along the three primary lattice directions, with the lowest along the direction where the lithium layers and the cobalt oxide layers alternate. The thermal conductivities is dependent on temperature, decreasing by about 60.33% from 300 °C to 400 °C and by about 53.31% from 400 °C to 500 °C. Additionally, strong size effects are identified which can be well characterized by Eq. (11) indicating a $1/\kappa - 1/L$ correlation. For polycrystalline $LiCoO_2$, the thermal conductivity becomes more isotropic and the dominant factor among others is the grain size. As the grain size varies from 2 nm to 4 nm, the thermal conductivity is increased from about 4.06 W m^{-1} K^{-1} to 9.08 W m^{-1} K^{-1}. The revealed grain size dependence is fundamentally due to two reasons, i.e. size effects of intra-grain thermal conductivities and thermal resistance of grain boundaries. In studying the grain boundary thermal resistance, one of the two grains forming the grain boundary is rotated to sample different relative orientations as seen in realistic grain boundaries. The axis about which the grain is rotated does not show significant influence. Rather, the tilt angle plays a dominant role, making the grain boundary thermal conductance vary in a wide range of 7.16 ~ 25.21 GW m^{-2} K^{-1}. All of these results contribute to the calibration of two thermal resistance models, i.e. Eq. (12) and Eq. (13). The two models use the same approach to include the contribution made by grain boundaries, but they treat size effects of intra-grain thermal conductivities differently. The first uses the size effects as revealed by Eq. (11), while the second uses the phonon kinetic theory with $\lambda_{grain}^{-1} = \lambda_0^{-1} + d^{-\alpha}$. Both models show consistent $\kappa_{poly} - d$ relationship. They collectively provide useful insights into the grain size effect within and beyond the nanocrystalline regime and may contribute to materials design for improved thermal management of batteries.

CONFLICTS OF INTEREST

There are no conflicts to declare.

ACKNOWLEDGEMENTS

This work is financially supported by CAREER Award No. CBET-1751610 from the National Science Foundation. The authors would like to thank Dr. Zheyong Fan of Aalto University for fruitful discussion.

REFERENCES

1. M. Armand and J. M. Tarascon, *Nature*, 2008, **451**, 652.
2. Y. Shao-Horn, L. Croguennec, C. Delmas, E. C. Nelson and M. A. O'Keefe, *Nature Materials*, 2003, **2**, 464.
3. Y. Zhou, S. Xiong, X. Zhang, S. Volz and M. Hu, *Nature Communications*, 2018, **9**, 4712.
4. B. Koo, P. Goli, A. V. Sumant, P. C. dos Santos Claro, T. Rajh, C. S. Johnson, A. A. Balandin and E. V. Shevchenko, *ACS Nano*, 2014, **8**, 7202-7207.
5. J. Wu, S. Yang, W. Cai, Z. Bi, G. Shang and J. Yao, *Scientific Reports*, 2017, **7**, 11164.
6. J. B. Bates, N. Dudney, B. J. Neudecker, F. X. Hart, H. P. Jun and S. A. Hackney, *Preferred Orientation of Polycrystalline LiCoO2 Films*, 2000.
7. A. Bodapati, P. K. Schelling, S. R. Phillpot and P. Keblinski, *Physical Review B*, 2006, **74**, 245207.
8. A. Bodapati, P. Keblinski, P. K. Schelling and S. R. Phillpot, *Applied Physics Letters*, 2006, **88**, 141908.
9. S. Ju and X. Liang, *Journal of Applied Physics*, 2012, **112**, 064305.
10. S. Ju and X. Liang, *Journal of Applied Physics*, 2010, **108**, 104307.
11. B. Mortazavi, M. Pötschke and G. Cuniberti, *Nanoscale*, 2014, **6**, 3344-3352.
12. B. Feng, Z. Li and X. Zhang, *Journal of Applied Physics*, 2009, **105**, 104315.
13. M. A. Meyers, A. Mishra and D. J. Benson, *Progress in Materials Science*, 2006, **51**, 427-556.
14. C.-W. Nan and R. Birringer, *Physical Review B*, 1998, **57**, 8264-8268.
15. H.-S. Yang, G. R. Bai, L. J. Thompson and J. A. Eastman, *Acta Materialia*, 2002, **50**, 2309-2317.
16. M. Maldovan, *Journal of Applied Physics*, 2011, **110**, 034308.

17. H. Dong, B. Wen and R. Melnik, *Scientific Reports*, 2014, **4**, 7037.
18. F. Fritzen, T. Böhlke and E. Schnack, *Computational Mechanics*, 2009, **43**, 701-713.
19. J. Schiøtz, F. D. Di Tolla and K. W. Jacobsen, *Nature*, 1998, **391**, 561.
20. F. X. Hart and J. B. Bates, *Journal of Applied Physics*, 1998, **83**, 7560-7566.
21. G. V. Lewis and C. R. A. Catlow, *Journal of Physics C: Solid State Physics*, 1985, **18**, 1149-1161.
22. S. Plimpton, *Journal of Computational Physics*, 1995, **117**, 1-19.
23. Y. Qi, L. G. Hector, C. James and K. J. Kim, *Journal of The Electrochemical Society*, 2014, **161**, F3010-F3018.
24. L. Wu, W. H. Lee and J. Zhang, *Materials Today: Proceedings*, 2014, **1**, 82-93.
25. L. Wu and J. Zhang, *Journal of Applied Physics*, 2015, **118**, 225101.
26. J. Cho, M. D. Losego, H. G. Zhang, H. Kim, J. Zuo, I. Petrov, D. G. Cahill and P. V. Braun, *Nature Communications*, 2014, **5**, 4035.
27. M. S. Green, *The Journal of Chemical Physics*, 1954, **22**, 398-413.
28. R. Zwanzig, *Annual Review of Physical Chemistry*, 1965, **16**, 67-102.
29. F. Müller-Plathe, *The Journal of Chemical Physics*, 1997, **106**, 6082-6085.
30. P. K. Schelling, S. R. Phillpot and P. Keblinski, *Physical Review B*, 2002, **65**, 144306.
31. Z. Wang and X. Ruan, *Journal of Applied Physics*, 2017, **121**, 044301.
32. A. J. H. McGaughey and M. Kaviany, *International Journal of Heat and Mass Transfer*, 2004, **47**, 1783-1798.
33. A. J. H. McGaughey and M. Kaviany, *International Journal of Heat and Mass Transfer*, 2004, **47**, 1799-1816.
34. H. M. Ledbetter, *Journal of Physics D: Applied Physics*, 1980, **13**, 1879-1884.
35. E. J. Cheng, N. J. Taylor, J. Wolfenstine and J. Sakamoto, *Journal of Asian Ceramic Societies*, 2017, **5**, 113-117.
36. A. Taube, J. Judek, A. Łapińska and M. Zdrojek, *ACS Applied Materials & Interfaces*, 2015, **7**, 5061-5065.
37. E. Langenberg, E. Ferreiro-Vila, V. Leborán, A. O. Fumega, V. Pardo and F. Rivadulla, *APL Materials*, 2016, **4**, 104815.
38. J. C. Duda, T. E. Beechem, J. L. Smoyer, P. M. Norris and P. E. Hopkins, *Journal of Applied Physics*, 2010, **108**, 073515.
39. C. Monachon, L. Weber and C. Dames, *Annual Review of Materials Research*, 2016, **46**, 433-463.
40. E. T. Swartz and R. O. Pohl, *Reviews of Modern Physics*, 1989, **61**, 605-668.
41. B. Mortazavi, L. F. C. Pereira, J.-W. Jiang and T. Rabczuk, *Scientific Reports*, 2015, **5**, 13228.
42. Z. Wang, J. E. Alaniz, W. Jang, J. E. Garay and C. Dames, *Nano Letters*, 2011, **11**, 2206-2213.